Influence of Reynolds Number on Vortex Flow over a Nonslender Delta Wing

Lan Chen,[*] Jinjun Wang,[†] Lin-xuan Zuo,[‡] and Li-hao Feng[§]

Beijing University of Aeronautics and Astronautics, 100191 Beijing, People's Republic of China

Through computational simulations performed for a 50° sweep delta wing at low Reynolds numbers $Re = 8.7 \times 10^3 - 4.0 \times 10^4$, this paper presents the features of the flow structures over the delta wing including the separated vortical flow, the onset of vortex breakdown, surface flow features, and dual vortex phenomena. At the lowest Reynolds number $Re = 8.7 \times 10^3$, no dual vortex structures are observed. As the Reynolds number is increased the dual vortex structures are developed, and the spanwise location of the vortex core is moved toward outboard without obvious variation of the vortex core vertical location above the wing leeward surface. At the lower Reynolds numbers investigated, the vortex breakdown location moves upstream as the Reynolds number increases. The primary reattachment lines move outboard toward the leading edge with the increasing Reynolds number, and simultaneously the start point of the secondary separation moves forward toward the tip of delta wing.

Nomenclature

b	=	semispan
C_p	=	pressure coefficient
c	=	chord length
h	=	height
Re	=	Reynolds number based on the chord length
t	=	wing thickness
U_{core}	=	axial velocity of the vortex core
U_{free}	=	freestream velocity
x	=	chordwise distance
x_c	=	vortex axis distance
y	=	spanwise distance
y_{le}	=	local semipan
z	=	normal (to the wing surface) distance
α	=	angle of attack
Λ	=	leading-edge sweep angle

I. Introduction

THE low-to-moderate sweep ($\Lambda = 35$–55 deg) wing platforms are often used on unmanned combat air vehicle (UCAV) and micro air vehicle (MAV) configurations [1–4]. These vehicles operate in relatively low Reynolds number range; typically the Reynolds number is $Re = 10^4$–10^5 for MAVs, and $Re = 10^5$–10^6 for an UCAV. In recent years, some investigations have been made into the flow over the nonslender delta wing at low Re [5–13].

Previous works have found that vortex flows and breakdowns are insensitive to the Re, so long as the slender wing leading edge is sharp [14–16]. However, Re has significant influence on the flow characteristics of nonslender delta wings, especially at low Re. A series of tests were conducted by Wang and Zhang [17] to examine the effects of sweep angle ($\Lambda = 45$ to 65 deg) and Re on vortex flow, which indicated that Re played an important role in the process of dual vortex structure formation, whereas Re was low, the dual vortex structures were not observed. Moreover, the lower the Re is, the larger the vortex breakdown onset angle would be. Taylor et al. [8] provided the water tunnel experimental results of vortex flow over nonslender delta wing with $\Lambda = 50°$ and $Re = 4.3 \times 10^3 - 3.47 \times 10^4$, their investigation showed that as Re decreased, the onset of breakdown was noticeably delayed, and the trajectory of the vortex core moved inboard toward the wing centerline. Gordnier and Visbal [6] have proposed a sixth-order compact differencing scheme and applied to the simulation of a low-sweep delta wing flow, and an initial assessment of Re effect was performed at $\alpha = 5°$. Their computational results for $Re = 10,000$, 20,000, and 50,000 showed that the viscosity have a significant influence on the development of the vortex structures.

Although there has been some recent research in the field for flow over nonslender delta wings, the literature concerning the effect of Re on the vortex flow is relatively less. Because of low Re considered, most of the previous works were conducted in a water tunnel and flow visualization was used to visualize the vortex trajectory and breakdown location. In this paper, we want to take advantage of the numerical simulation to facilitate a better understanding of the vortex flow over a thin flat sharp-edged delta wing with $\Lambda = 50°$, including the behavior of the leading-edge vortex, vortex breakdown and surface flow features. Special emphasis is paid on the effect of Re between $Re = 8.7 \times 10^3$ and $Re = 4.0 \times 10^4$. The velocity field was measured in a recirculation water tunnel in Beijing University of Aeronautics and Astronautics (BUAA) with a digital particle image velocimetry (PIV) to help and deepen the understanding of vortex flow over nonslender delta wing at low Re.

II. Computation and Experimental Setup

Figure 1 shows the thin-plate delta wing with a leading-edge sweep angle of $\Lambda = 50°$, a thickness to chord ratio of $t/c = 2.25\%$ and a 45° windward side bevels on the leading edge. The x coordinate defines the centerline, y the spanwise direction and U_{core} the axial velocity component along the vortex axis x_c. The flowfield is assumed to be symmetric about the centerline of the delta wing, therefore only half of the delta wing is considered in the simulation, and all of the computations are performed under laminar.

The unsteady compressible three-dimensional Navier–Stokes equations are chosen to properly model the complex vortex flow over delta wing. The governing equations are expressed in the generalized curve coordinates, that is

---

*Fluid Mechanics Key Laboratory. Currently, Associated Research Scientist, China Aerodynamics Research and Development Center, Mianyang, 62100 Sichuan; hhd_cll@163.com.

†Professor, Fluid Mechanics Key Laboratory; jjwang@buaa.edu.cn (Corresponding Author). Member AIAA.

‡Graduate Student, Fluid Mechanics Key Laboratory; zuoeddie@ase.buaa.edu.cn.

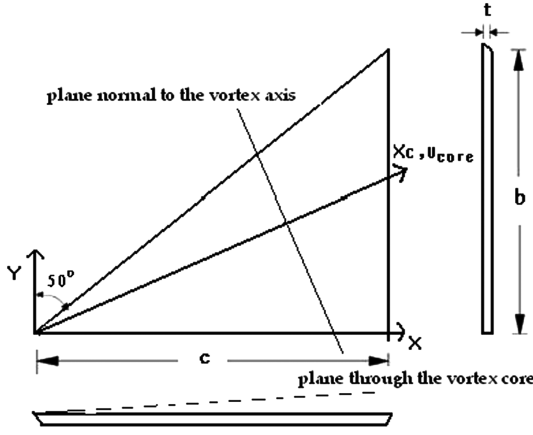§Graduate Student, Fluid Mechanics Key Laboratory; skyyds8@163.com.

Fig. 1 Schematic of delta wing.

$$\frac{\partial \hat{U}}{\partial t} + \frac{\partial \hat{E}}{\partial \xi} + \frac{\partial \hat{F}}{\partial \eta} + \frac{\partial \hat{G}}{\partial \zeta} = \frac{\partial \hat{E}_v}{\partial \xi} + \frac{\partial \hat{F}_v}{\partial \eta} + \frac{\partial \hat{G}_v}{\partial \zeta} \qquad (1)$$

With this formulation, the vector notations are given as follows:

$$\hat{U} = J^{-1} U$$
$$\hat{E} = J^{-1}(\xi_t U + \xi_x E + \xi_y F + \xi_z G)$$
$$\hat{F} = J^{-1}(\eta_t U + \eta_x E + \eta_y F + \eta_z G)$$
$$\hat{G} = J^{-1}(\zeta_t U + \zeta_x E + \zeta_y F + \zeta_z G)$$
$$\hat{E}_v = J^{-1}(\xi_x E_v + \xi_y F_v + \xi_z G_v)$$
$$\hat{F}_v = J^{-1}(\eta_x E_v + \eta_y F_v + \eta_z G_v)$$
$$\hat{G}_v = J^{-1}(\zeta_x E_v + \zeta_y F_v + \zeta_z G_v)$$

Here U is the vector of conserved variables and J denotes the transformation Jacobian. E, F, G are inviscid fluxes, and E_v, F_v, G_v are viscous fluxes.

A semidiscrete finite volume method is employed to solve the governing equations. The second-order Roe scheme [18] is adopted for the spatial discretization of the inviscid fluxes. The viscous flux terms are discretized by second-order central differences. Time advancement uses the dual time-stepping method. This technique introduces an outer time-stepping loop for a real time step employing an implicit scheme, and an inner loop with a fictitious time step to reach the *steady state* at each real time step. The numerical scheme has second-order spatial and temporal accuracy.

For the nonmoving grid, Eq. (1) may be written as

$$\frac{1}{J} \frac{\partial U}{\partial t} = R(U) \qquad (2)$$

where $R = -[\frac{\partial(\hat{E}-\hat{E}_v)}{\partial \xi} + \frac{\partial(\hat{F}-\hat{F}_v)}{\partial \eta} + \frac{\partial(\hat{G}-\hat{G}_v)}{\partial \zeta}]$. A fictitious time term is added to Eq. (2)

$$\frac{1}{J} \frac{\partial U}{\partial \tau} + \frac{1}{J} \frac{\partial U}{\partial t} = R(U) \qquad (3)$$

where t denotes the real time and τ is fictitious time. If the subiteration converges, the fictitious time term vanishes and Eq. (3) once again becomes Eq. (2).

This equation is then discretized to achieve second-order temporal accuracy. The scheme can be written as

$$\frac{1}{J \Delta \tau}(U^{m+1} - U^m) + \frac{1}{J \Delta t}\left[\frac{3}{2}(U^{m+1} - U^n)\right.$$
$$\left. - \frac{1}{2}(U^n - U^{n-1})\right] = R(U^{m+1}) \qquad (4)$$

m is the subiteration counter. Let $\Delta U^m = U^{m+1} - U^m$, and add quantity $-\frac{1}{J\Delta t}\frac{3}{2}U^m$ to both sides of Eq. (4). Equation (4) becomes

$$\frac{1}{J\Delta \tau}\Delta U^m + \frac{1}{J\Delta t}\frac{3}{2}\Delta U^m = -\frac{1}{J\Delta t}\frac{3}{2}U^m + \frac{1}{J\Delta t}\frac{3}{2}U^n$$
$$+ \frac{1}{2}\frac{1}{J\Delta t}\Delta U^{n-1} + R(U^{m+1}) \qquad (5)$$

If $R(U^{m+1})$ is linearized by $R(U^{m+1}) = R(U^m) + (\frac{\partial R}{\partial U})^m \Delta U^m$

$$\frac{\partial R}{\partial U} = -\frac{\partial}{\partial U}\left[\frac{\partial(\hat{E}-\hat{E}_v)}{\partial \xi} + \frac{\partial(\hat{F}-\hat{F}_v)}{\partial \eta} + \frac{\partial(\hat{G}-\hat{G}_v)}{\partial \zeta}\right]$$
$$= -\frac{\partial}{\partial \xi}\left[\frac{\partial(\hat{E}-\hat{E}_v)}{\partial U}\right] - \frac{\partial}{\partial \eta}\left[\frac{\partial(\hat{F}-\hat{F}_v)}{\partial U}\right] - \frac{\partial}{\partial \zeta}\left[\frac{\partial(\hat{G}-\hat{G}_v)}{\partial U}\right]$$
$$= -\frac{\partial A}{\partial \xi} - \frac{\partial B}{\partial \eta} - \frac{\partial C}{\partial \zeta}$$

Where $A = \frac{\partial(\hat{E}-\hat{E}_v)}{\partial U}$, $B = \frac{\partial(\hat{F}-\hat{F}_v)}{\partial U}$, $C = \frac{\partial(\hat{G}-\hat{G}_v)}{\partial U}$.
Then Eq. (5) becomes

$$\left(\frac{1}{J\Delta \tau} + \frac{1}{J\Delta t}\frac{3}{2} + \frac{\partial A}{\partial \xi} + \frac{\partial B}{\partial \eta} + \frac{\partial C}{\partial \zeta}\right)\Delta U^m$$
$$= -\frac{1}{J\Delta t}\frac{3}{2}U^m + \frac{1}{J\Delta t}\frac{3}{2}U^n + \frac{1}{2}\frac{1}{J\Delta t}\Delta U^{n-1} + R(U^m) \qquad (6)$$

Equation (6) is solved using the approximately factored scheme, that is

$$\left(\frac{1}{J\Delta \tau} + \frac{1}{J\Delta t}\frac{3}{2} + \frac{\partial A}{\partial \xi}\right)\Delta U' = \frac{1}{2}\frac{1}{J\Delta t}\Delta U^{n-1}$$
$$- \frac{1}{J\Delta t}\frac{3}{2}(U^m - U^n) + R(U^m) \qquad (7)$$

$$\left(\frac{1}{J\Delta \tau} + \frac{1}{J\Delta t}\frac{3}{2} + \frac{\partial B}{\partial \eta}\right)\Delta U'' = \left(\frac{1}{J\Delta \tau} + \frac{1}{J\Delta t}\frac{3}{2}\right)\Delta U' \qquad (8)$$

$$\left(\frac{1}{J\Delta \tau} + \frac{1}{J\Delta t}\frac{3}{2} + \frac{\partial C}{\partial \zeta}\right)\Delta U^m = \left(\frac{1}{J\Delta \tau} + \frac{1}{J\Delta t}\frac{3}{2}\right)\Delta U'' \qquad (9)$$

Finally

$$U^{m+1} = U^m + \Delta U^m \qquad (10)$$

As $m \to \infty$, $\frac{1}{J}\frac{\partial U}{\partial \tau} \to 0$ and $U^{m+1} \to U^{n+1}$.

To improve the understanding of the inner structure and behavior of the vortex breakdown, the PIV experiment was carried out in a circuit water tunnel at the BUAA, which has a $4.8 \times 0.6 \times 0.6$ m test section. Both of sidewalls are made of plexiglass to allow flow visualization viewing from the sides as well as from above. An aluminum low-sweep angle delta wing model ($\Lambda = 50°$) was supported by a vertical strut underneath the wing surface. The freestream velocity was 0.084 m/s, resulting in $Re = 1.2 \times 10^4$ based on the root chord length $c = 0.15$ m. The angles of attack $\alpha = 5, 8, 11$, and $15°$ were considered.

A two-dimensional digital particle image velocimetry technique was applied for taking the advantage of both continuous laser and high-speed CCD camera designed to fulfill the sequence measurement of low-speed flow. The laser sheet is generated with a maximum energy output of 1.5 W and thickness of 1 mm. Hollow glass particles of 1.05 g/mm³ specific gravity and 5 μm diameter are used as tracker particles. The high-speed charge-coupled device (CCD) camera has an array of 640×480 pixels with maximum capture rate of 200 frames per second. A maximum of 10,000 images can be recorded at one time. The physical size of the interrogation domain was 0.08×0.06 m.

The velocity field in a plane through the vortex core was measured using the PIV. To identify the leading-edge vortex core locations, dye was injected into the flow near the apex of the model. The laser sheet was aligned with the vortex core, which the CCD camera was placed normal to. The arrangement of the light sheet, camera and model is
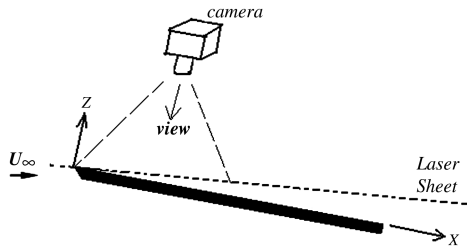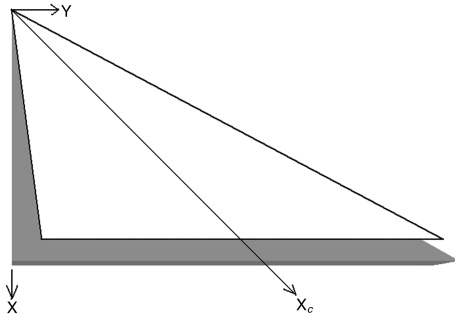
Fig. 2 Schematic of laser sheet orientation.

Fig. 3 Plane through the vortex core.

shown in Fig. 2. The plane through the vortex core corresponds to the PIV measurement plane, as shown in Fig. 3.

III. Results

Four H-O grids are developed to assess the grid resolution, which consist of $100 \times 119 \times 70$; $100 \times 239 \times 70$; $100 \times 279 \times 70$, $100 \times 359 \times 70$, in the axial, circumferential and normal direction, respectively. Mesh refinement is made in the spanwise direction over

the delta wing. Surface mesh and typical cross section of the grids are shown in Fig. 4a and 4b. A case of $\alpha = 8°$ and $Re = 274,000$ is computed to compare with the wind tunnel pressure measurement conducted by Lu [10] in BUAA. Figure 4c plots the surface pressure coefficient at two axial location, $x/c = 0.4$ and 0.6. The grid of $100 \times 119 \times 70$ is too coarse to capture the basic flow structure. Other three grids pressure distributions show similar features, exhibit pressure peak, also have small second peak outboard of the wing, and agree well with the experiment measurements except that pressure peak at $x/c = 0.4$ is slightly higher in the experiment. Then another case of $Re = 205,000$ is performed on the finer grid ($100 \times 279 \times 70$). Figure 4d shows the surface streamline pattern, including primary separation at the leading edge, attachment line (A1) and secondary separation (S2), which are similar with experimental oil flow pattern obtained by Verhaagen and Elsayed [13]. Figure 4e presents the locations of the primary attachment line at $x/c = 0.5$ for different α. Figure 4f shows the variations of lift and drag coefficient (C_L, C_D) with α. The computational results are consistent with the oil-flow visualization [13] and the balance measurement data [19]. Based on these initial investigations, all subsequent numerical simulations have been performed on the finer grid. The spacing on the wing is $\Delta x/c = 0.001$ in the streamwise direction, and $\Delta z/c = 0.0001$ in the normal direction near the surface.

A. Leading-Edge Vortices

Numerical simulations in this work are performed at $Re = 8.7 \times 10^3$, 1.3×10^4, 2.6×10^4, and 4.0×10^4, and $\alpha = 2, 5, 8, 11$, and $15°$ are considered. Figure 5 presents the three flow patterns on the leeward field of delta wing: 1) a thick separated shear layer emanates from the leading edge without the presence of any concentrated vortex structure, as shown in Fig. 5a; 2) the flow separates from the leading edge to develop a steady leading-edge vortex when it attaches on the wing, as shown in Fig. 5b; 3) another concentrated vortex, with the same rotated direction as the primary vortex, emerges outside the primary leading-edge vortex, forming a dual vortex structure, as shown in Fig. 5c. Figure 5d shows the
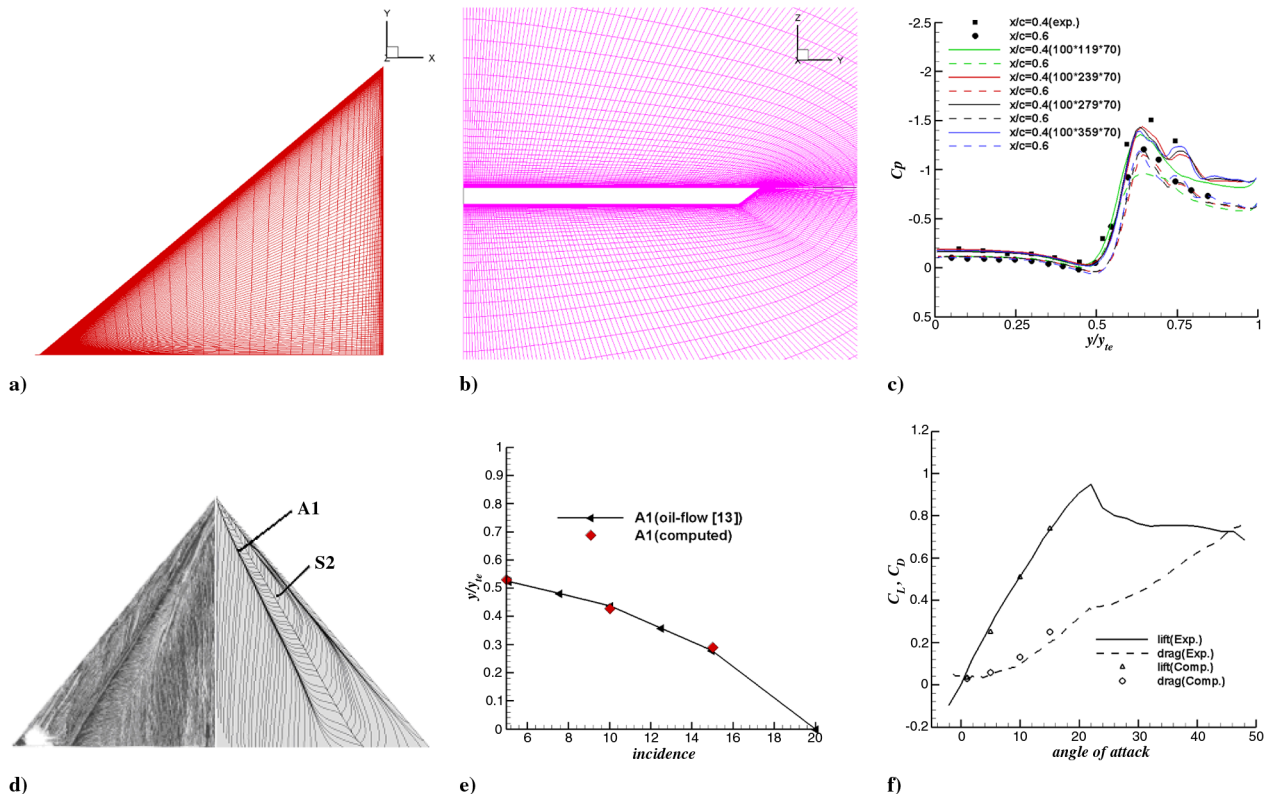

Fig. 4 Schematics of a) surface grid, b) cross section, and c) surface pressure at $x/c = 0.4, 0.6$. Part d) $\alpha = 5°$; left: oil flow pattern [13], right: surface streamline pattern. Part e) locations of primary attachment line as a function of α, and part f) variation of lift and drag coefficients with α.
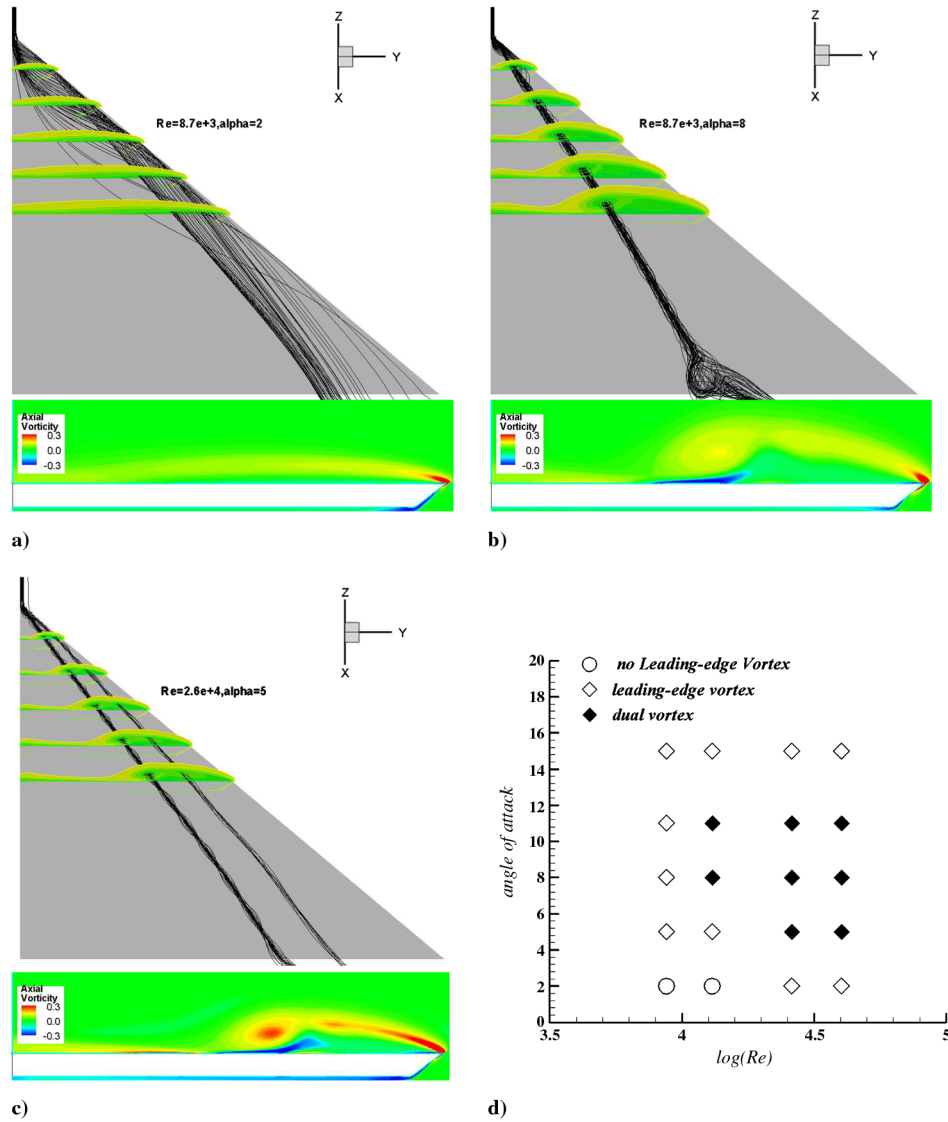
Fig. 5   Schematics of a) separated shear layer, b) single leading-edge vortex, c) dual-vortex structure, and d) flow patterns.

variation of the main flow phenomena over a 50° delta wing as a function of Re at $\alpha = 2, 5, 8, 11$, and $15°$, where the influence of Re is obvious. If Re is too low, the dual vortex structures cannot be formed. At the lowest $Re = 8.7 \times 10^3$, no dual vortex structure was developed. Wang and Zhang [17] found that no dual vortex structure was observed in their flow visualization experiment for $Re = 6.0 \times 10^3$. With the increase of Re, the onset α, at which the dual vortex structures appear first, is gradually reduced. When Re is larger than 10^4, the increase of α results in the variation of flow patterns from the formation of steady LEV to the appearance of dual vortex structure, and finally back to the single leading-edge vortex.

B.   Vortex Core Trajectories

The dependences of Re and α on the vortex core trajectories can be defined in term of the vertical and spanwise locations of the vortex core. Figures 6a and 6b shows the distance of vortex core away from the leeward surface vs α and Re, respectively. The core moves away from the model surface as α is increased as shown in Fig. 6a, however, the effect of Re is less apparent as shown in Fig. 6b. Wang and Zhang [17] concluded that for nonslender delta wing, Re has no significant influence on the angle between the delta wing surface and the leading-edge vortex core, this is consistent with our present computational results.
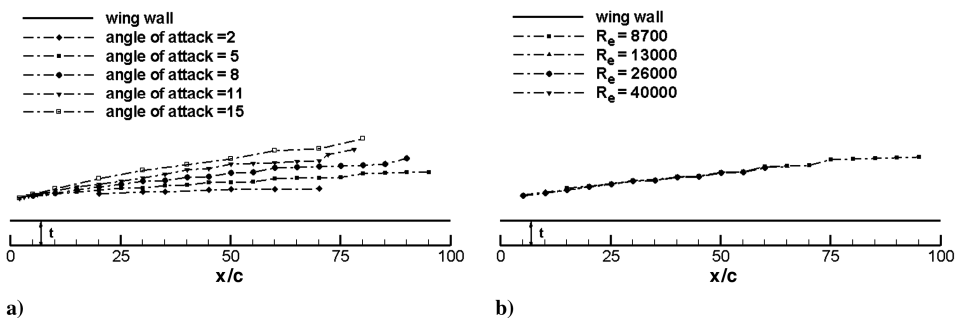

Fig. 6   Schematics of a) variations of vortex height with α at $Re = 2.6 \times 10^4$, and b) variations of vortex height with Re at $\alpha = 8°$.
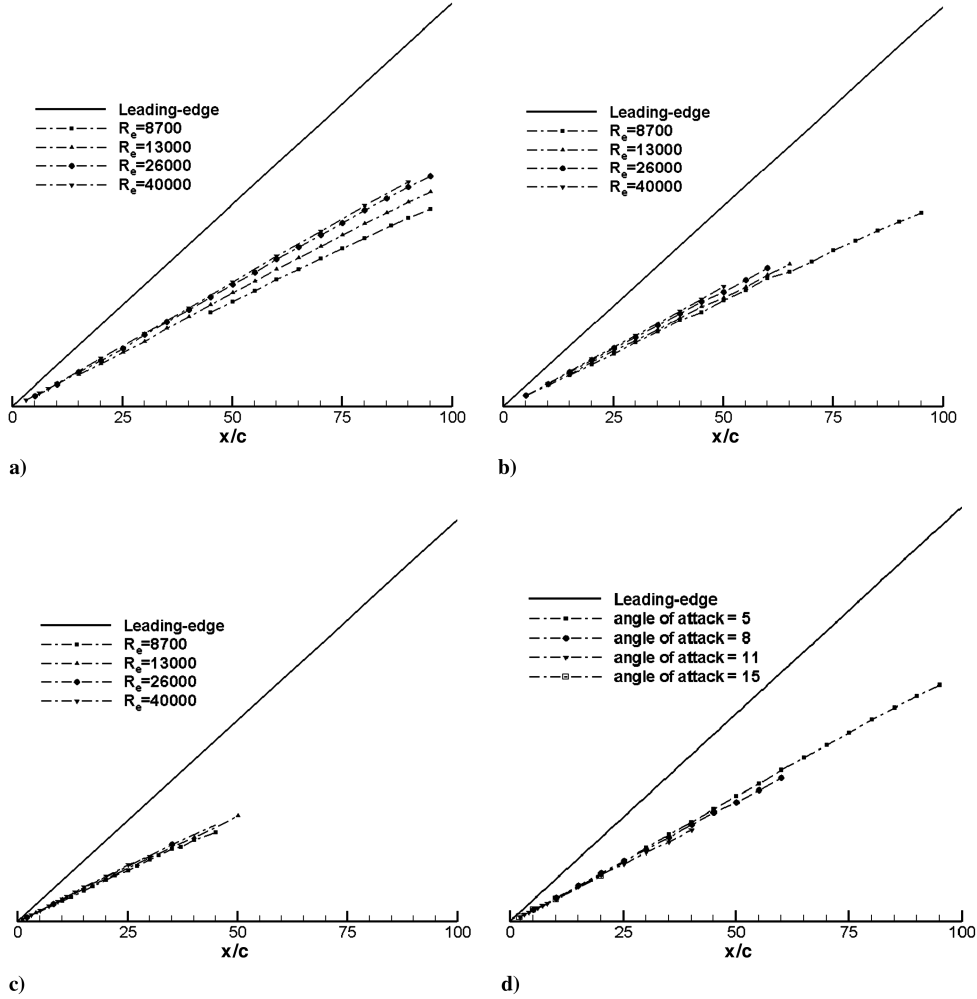
Fig. 7 Schematics of a) variations of the spanwise locations of vortex core with Re at $\alpha = 5°$, b) variations of the spanwise locations of vortex core with Re at $\alpha = 8°$, c) variations of the spanwise locations of vortex core with Re at $\alpha = 11°$, and d) variations of the spanwise locations of vortex core with α at $Re = 2.6 \times 10^4$.

Although the vertical location of the vortex core is insensitive to Re, the spanwise location is not the same as shown in Figs. 7a–7c. It is observed that the vortex cores move away from the centerline toward the leading edge with increasing Re. The effect of Re increases with α, such a phenomenon is more apparent at a lower α ($\alpha = 5°$, Fig. 7a) than a higher value ($\alpha = 11°$, Fig. 7c). The vortex cores tend to move toward the centerline as α is increased as shown in Fig. 7d.

Both the results of computations and flow visualization experiments [8,17] show consistently that the spanwise location of the vortex core is related to Re. The effect of Re on the spanwise location of the vortex core is opposite to that of α [17].

C. Vortex Breakdown

Vortex breakdown is an important phenomenon of delta wing featured by the sudden slowdown of axial flow and expansion of vortex core diameter [20], and it is not very easy to define exactly the location of breakdown. For flow visualization experiment, the breakdown locations are identified by observation the abrupt change
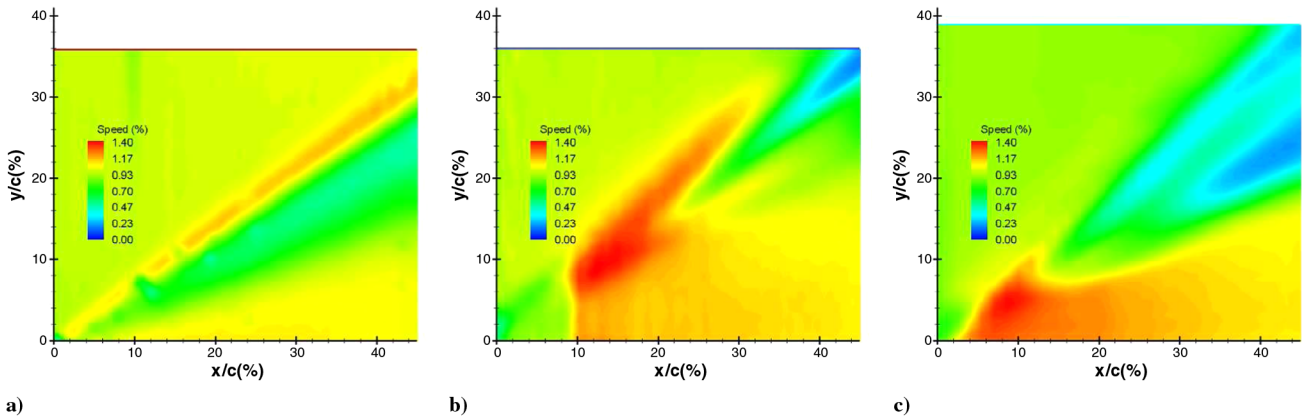

Fig. 8 PIV measurements of the velocity magnitude on a plane through the vortex core, $Re = 1.2 \times 10^4$: a) $\alpha = 5°$, b) $\alpha = 11°$, and c) $\alpha = 15°$.
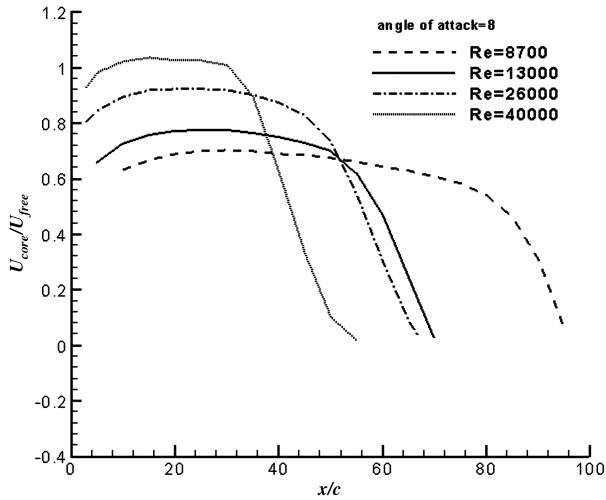
Fig. 9   Effect of *Re* on axial velocity along the vortex core.

45% of the chord length, as shown in Fig. 8b. Further increasing α to 15°, the vortex breakdown occurs at about one-third of the root chord length from the wing apex as shown in Fig. 8c. The vortex breakdown region moves toward the wing apex with increasing α, this is similar to vortex breakdown over slender delta wing.

For the numerical flowfield, inspection of axial velocity distribution can present a better realization of the breakdown location. When breakdown occurs, the axial flow stagnates and a region of reverse flow develops. Figure 9 shows the effects of *Re* on the axial velocity along vortex core. It is obvious from Fig. 9 that the positions of vortex breakdown are also strongly affected by *Re*. At the lowest Reynolds number of $Re = 8700$, vortex breakdown occurs at a little upstream of the trailing edge. As the Reynolds number is increased to $Re = 4.0 \times 10^4$, the vortex breakdown location is at downstream of one half of the root chord length, as shown in Fig. 9. The trend that the vortex breakdown moves towards upstream with increasing *Re* agrees with that in the previous experimental studies [3,8,17].

D.   Surface Flow Features

The impact of *Re* on the nonslender delta wing can also be described by the surface flow topology. Figure 10 displays the surface limiting streamlines at $\alpha = 5°$ for $Re = 8.7 \times 10^3$, 1.3×10^4, 2.6×10^4 and 4.0×10^4. In these figures, S1, S2 denote the primary separation and secondary separation lines, respectively. A1, A2 denote the primary attachment and secondary attachment lines, respectively. S1 occurs at the leading edge of the delta wing. The locations of vortex axis are marked with dotted red line. Comparison of the results shown in Fig. 10 suggests that the onset of the secondary separation and attachment lines shift upstream to the apex of wing with increasing Reynolds number. At the lowest Reynolds number $Re = 8.7 \times 10^3$, the secondary separation occurs at the downstream location; however, as Reynolds number is raised to $Re = 4.0 \times 10^4$, the secondary separation moves to near the wing apex.

in the structure of the vortex. When breakdown occurs, the ordered straight streak lines expand or twist suddenly. This method is more qualitative. PIV measurement can exhibit the basic features for the breakdown structure. Figure 8 shows the results of PIV measurement for velocity contour of the plane through the vortex core. The measuring plane covered a distance of 45% chord length. The leading-edge vortex at $\alpha = 5°$ is not strong but remains steady, as shown in Fig. 8a. When α is increased, the onset of vortex breakdown occurs, and the velocity decreases. It is noted that the axial velocity decelerates gradually through a breakdown region, instead of dropping abruptly at one point. This is the characteristic of vortex breakdown for the nonslender delta wing [4,6]. The position of breakdown is located for $\alpha = 8°$ from $x/c = 60\%$ to $x/c = 70\%$. For $\alpha = 11°$, the vortex breakdown region moves upstream to nearly
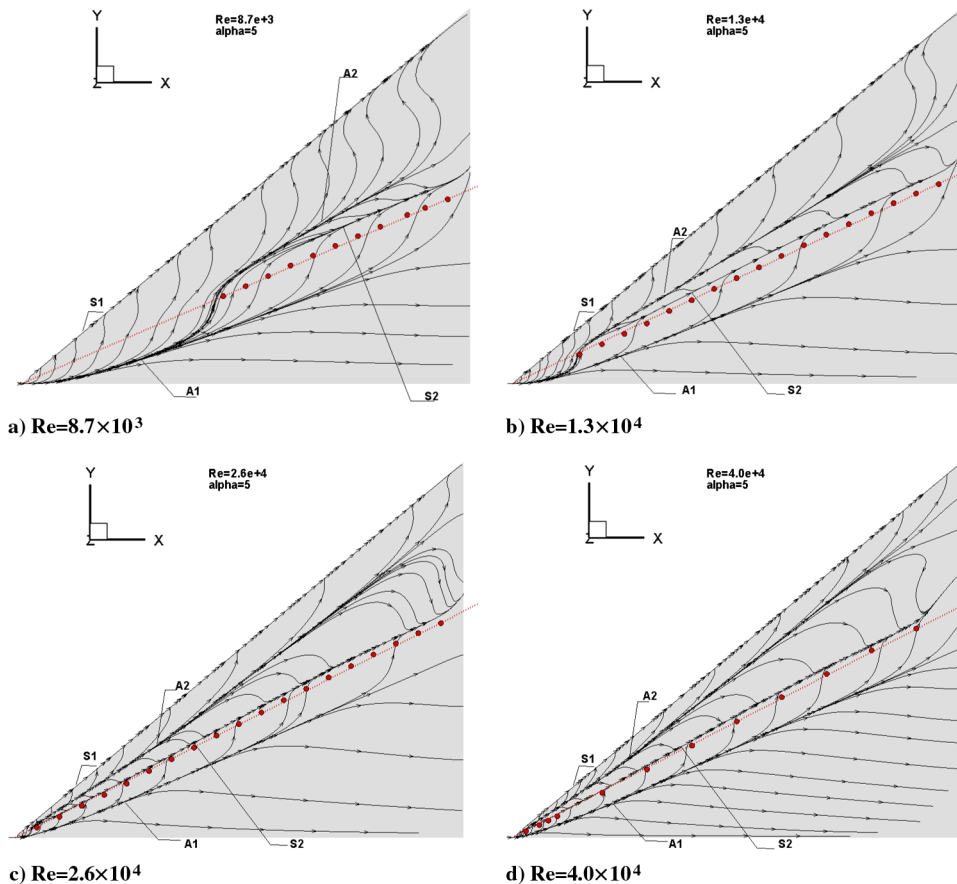

a) Re=8.7×10³

b) Re=1.3×10⁴

c) Re=2.6×10⁴

d) Re=4.0×10⁴

Fig. 10   Surface limiting streamlines at $\alpha = 5°$.

Table 1 Separation, attachment, and axis location

$y/y_{le(\%)}$ Re		$x/c = 0.3$				$x/c = 0.5$		
		A1	S2	A2	X_c	A1	S2	A2	X_c
8.7×10^3	25.93				33.2			52.00
1.3×10^4	33.46	60.64	68.56	53.43	39.10	60.50	69.67	56.30
2.6×10^4	41.39	61.84	76.80	59.07	46.08	63.74	81.70	60.49
4.0×10^4	43.63	63.45	82.73	60.46	48.63	65.65	87.82	61.85

The relative spanwise locations of the primary attachment (A1), secondary separation (S2), secondary attachment (A2) and vortex core at the axial locations $x/c = 0.3$, 0.5 are given in Table 1; y_{le} is the local semispan. From Table 1, we can see that the primary attachment point, the secondary separation and attachment points move outward to the leading edge and the width of the primary vortex footprint narrows as Re increases.

The variations of surface flow patterns become much more complicated when α is increased. Figure 11 shows the surface limiting streamlines at $\alpha = 11°$ for different Re. In this figure the
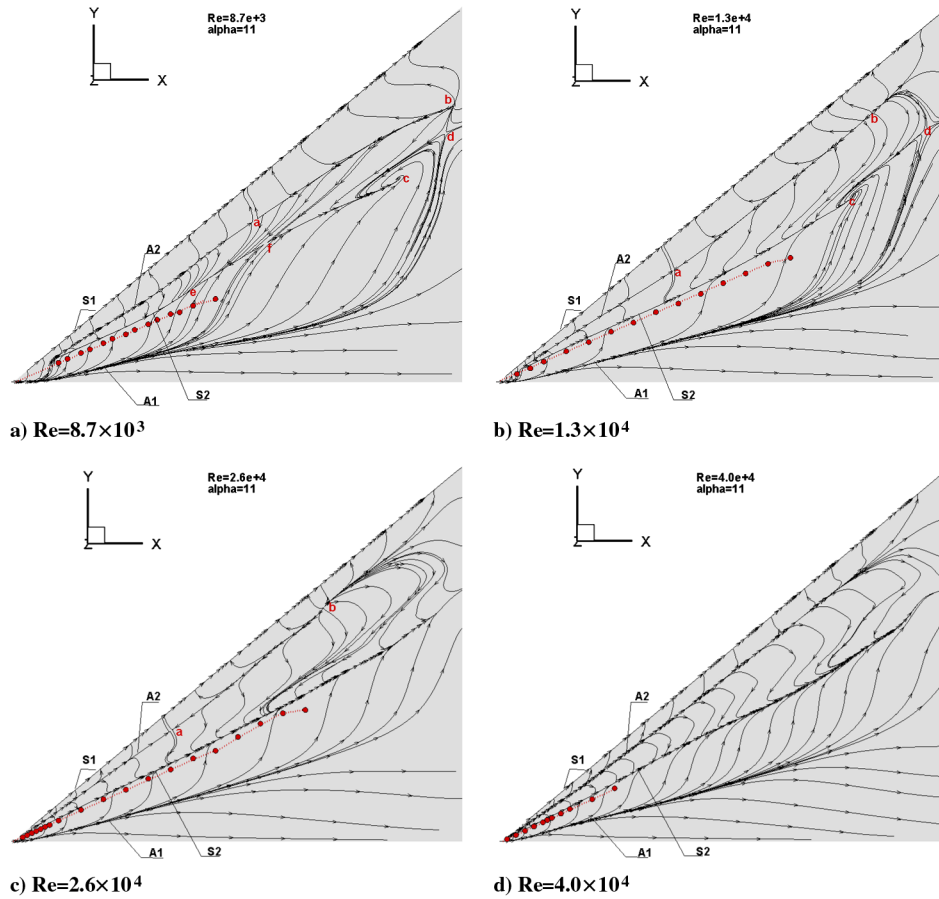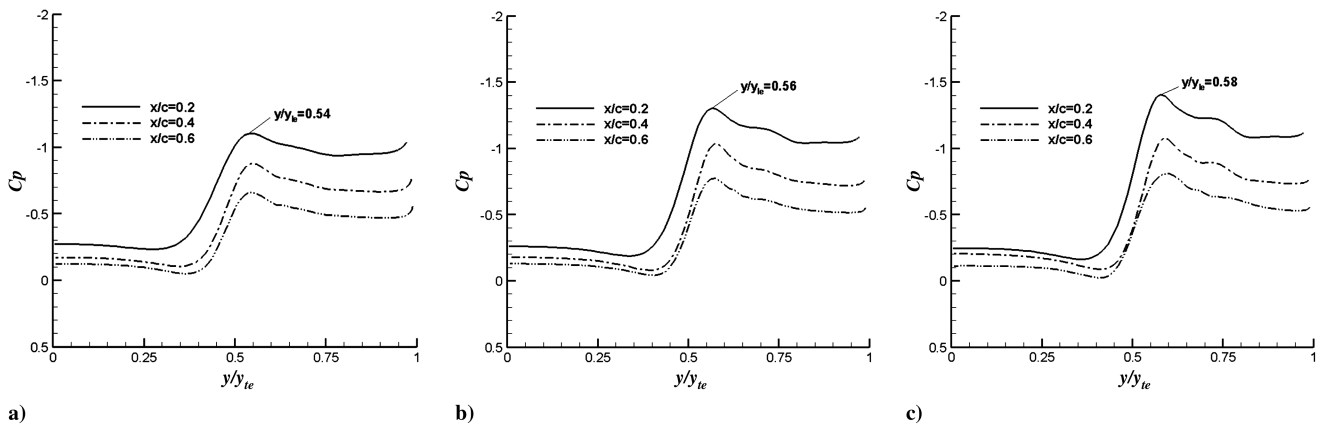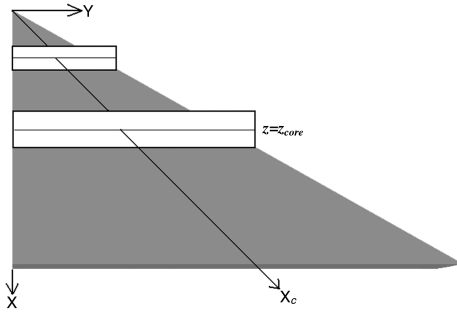

a) Re=8.7×10³

b) Re=1.3×10⁴

c) Re=2.6×10⁴

d) Re=4.0×10⁴

Fig. 11 Surface limiting streamlines, $\alpha = 11°$.

a)

b)

c)

Fig. 12 Surface pressure coefficient at $x/c = 0.2, 0.4, 0.6, \alpha = 8°$: a) $Re = 1.3 \times 10^4$, b) $Re = 2.6 \times 10^4$, and c) $Re = 4.0 \times 10^4$.

Table 2   Spanwise location of secondary vortex, dual vortex, and Cp-step

| | | $Re = 26{,}000$ | | | | $Re = 40{,}000$ | |
x/c	y_{sc}/y_{le} secondary vortex	y_{dc}/y_{le} dual vortex	$y_{Cp\text{-step}}/y_{le}$ Cp-step	y_{sc}/y_{le} secondary vortex	y_{dc}/y_{le} dual vortex	$y_{Cp\text{-step}}/y_{le}$ Cp-step
0.2	0.703	0.807	0.684–0.705	0.730	0.818	0.684–0.725
0.4	0.692	0.786	0.683–0.694	0.727	0.808	0.694–0.727

letters a, b, c, and d represent the critical points, which are classified according to the three-dimension separated flow theory [21] and the characteristic of surface limiting streamline [22]. Point a is a classical saddle point, which corresponds to the apparent intersections of surface streamlines. Point b is an attachment node, away from which the streamlines are oriented. The saddle and nodal point occur on the secondary attachment line A2, as shown in Figs. 11a–11c. Point c is a focus, which denotes a region of tightly wound, spiral-like

Fig. 13   Plane normal to the wing surface.

streamlines. Points d and f are the saddle points. Point e is separation node because the streamlines are oriented toward the node. For $Re = 8.7 \times 10^3$, the saddle and nodal points occur on the S2, alternately. As Re is raised to 1.3×10^4, one saddle and one nodal point occur on the A2 and S2, respectively (see Fig. 11b). Further increasing Re to 2.6×10^4, the saddle and nodal points only occur on the A2 near the leading edge (see Fig. 11c). Compared with the results in Figs. 11a–11c, there is no singular point in Fig. 11d, the surface flow pattern becomes simpler as Re is increased to 4.0×10^4. Figure 11 indicates that the lower the Re is, the more complicated the surface flow pattern is. Compared with Fig. 10, it is suggested that vortex breakdown has impact on the secondary separation line. At $\alpha = 5°$, S2 straights up to the trailing edge. When vortex breakdown occurs, S2 bends outboard due to an enlargement of vortex core (see Fig. 11).

E.   Pressure Distributions and Velocity Field

The above discussion demonstrates that Re has a significant influence on the flow structure of the nonslender delta wing. The effect of Re on surface pressure and velocity field is discussed in this section. Figure 12 illustrates surface pressure distributions for $\alpha = 8°$ at three

a) Re=8.7×10³

b) Re=1.3×10⁴

c) Re=2.6×10⁴
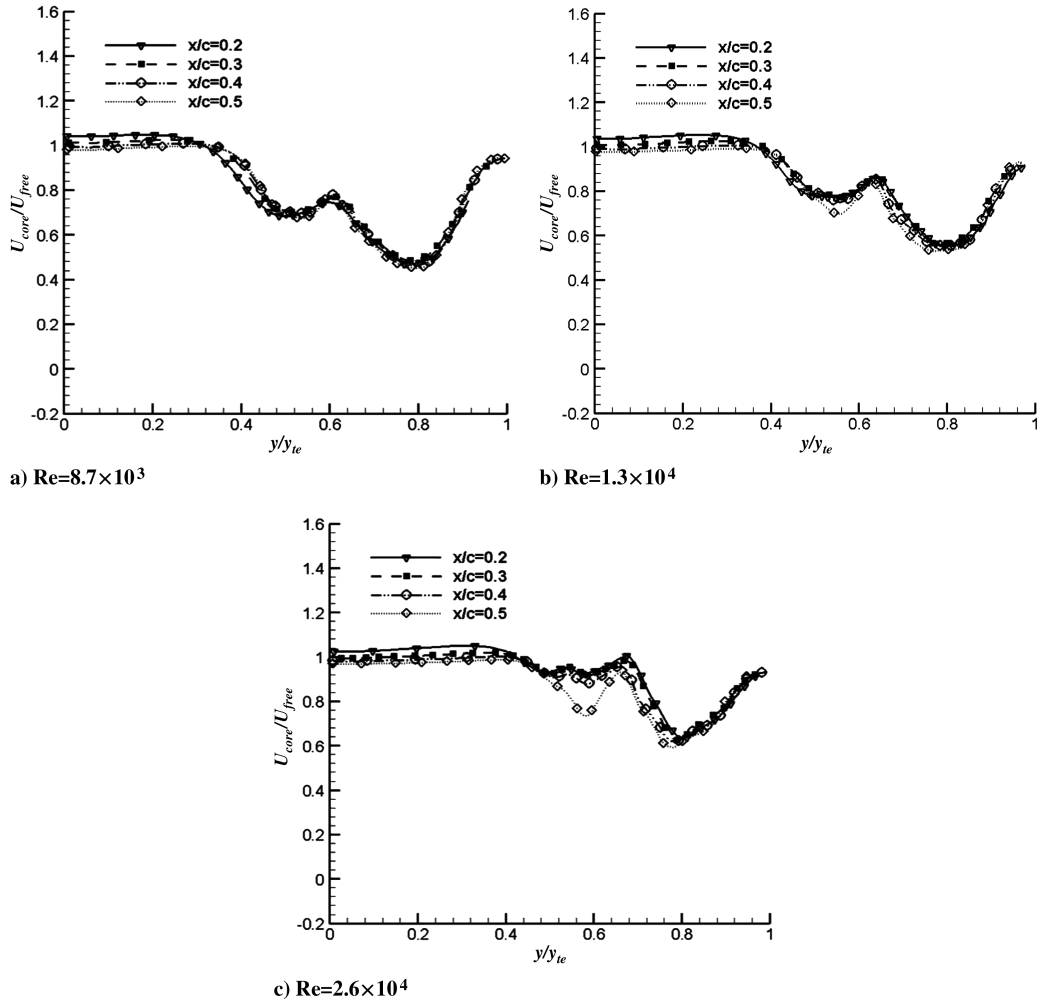
Fig. 14   Axial velocity distribution at $x/c = 0.2–0.5$, $\alpha = 8°$.

chord stations $x/c = 0.2, 0.4$ and 0.6, and $Re = 1.3 \times 10^4, 2.6 \times 10^4$ and 4.0×10^4. The peak suction pressure occurs near the same percentage of semispan for all pressure stations. We have noticed that the vortex cores remain straight as shown in Fig. 5b. Comparing the three results in Fig. 12, we can see that with increased Re, the peak suction pressure gradually increases and its spanwise position trends to move outboard appreciably, which is consistent with the results reported in Sec. III.B, the spanwise location of the vortex core also moves outboard away the centerline with increasing Re.

The small Cp-step outboard of suction peak is also visible in Figs. 12b and 12c. What is the curve step induced by? Table 2 lists the locations of the small Cp-step and the secondary vortex core, as well as that of the dual-primary vortex. For Fig. 12b, at $x/c = 0.2$, the pressure step locates at $y/y_{le} = 0.684$–0.705, the secondary vortex core at $y/y_{le} = 0.703$, and dual-primary vortex core at $y/y_{le} = 0.807$. It indicates that the Cp-step should be induced by the secondary vortex not dual vortex. Furthermore, increasing Re will result in a strengthening of the secondary vortex.

The measurements of Ol [5] for a $50°$ sweep delta wing at $Re = 8.5 \times 10^3$ suggested that the velocity field near the apex exhibited a generally conical development. To interpret the effect of Re on the velocity field, velocity profiles are plotted on the selected cross sections which are cut through the vortex core and normal to the wing leeward surface as shown in Fig. 13. Velocity profiles at $Re = 8.7 \times 10^3, 1.3 \times 10^4$, and 2.6×10^4 are presented in Fig. 14. At the lowest Re of 8.7×10^3, four velocity profiles at streamwise stations $x/c = 0.2, 0.3, 0.4$, and 0.5 are similar, that is, the velocity field on half of chord are near conical flow (Fig. 14a). When Re is tripled to $Re = 2.6 \times 10^4$, only two velocity profiles at $x/c = 0.2$ and 0.3 are similar (Fig. 14c). It is shown that the conical flow region is gradually shrinking with increasing Re. It can also be seen from Fig. 9 that the variation of axial velocity along the vortex core characterizes three stages, i.e., increasing, then reaching a plateau and rapid declining finally. When vortex core velocity remains fairly constant, the flowfield exhibits a conical development. As Re is increased, the width of the velocity plateau narrows, and the conical velocity field region decreases.

IV. Conclusions

Numerical simulations have been performed for a $50°$ sweep delta wing at low Reynolds number of $Re = 8.7 \times 10^3 - 4.0 \times 10^4$, and it is indicated that Re plays an important role in the vortex structure development over nonslender delta wing.

1) The Reynolds number has a significant influence on the vortex structure. If Re is too low, the dual vortex structures could not be formed. With the increase of Re, the primary vortex is formed at lower α, and the onset α, at which the dual vortex first appears, is decreased. Meanwhile, the primary reattachment line moves towards the leading edge, and the secondary separation point moves toward the apex of the model. Moreover, the width of primary vortex footprint decreases simultaneously.

2) The effect of Re on the location of primary vortex core is contrary to that of α. The trajectories of the vortex core move outboard toward the leading edge as the Re is increased, but tend to shift inboard toward the centerline as α is increased. The vortex core moves away from the model surface with increasing α, but it is insensitive to Re.

3) The Reynolds number has an effect on the position of the vortex breakdown. At the lower α, the breakdown location moves upstream as Re increases. Additionally, as Re is raised, the peak suction pressure is increased. At lower Re, the velocity field exhibits an approximate conical flow near the apex of the nonslender delta wing.

4) As α is increased, the core of the primary vortex gradually goes away from the wing surface and moves towards the centerline of the model.

Acknowledgments

References

[1] Gursul, I., Taylor, G., and Wooding, C. L., "Vortex Flows over Fixed-Wing Micro Air Vehicles," AIAA Paper 2002-0698, 2002.

[2] Russell M. Cummings, Scott, A. Morton, Stefan, G. Siegel, and Steven Bosscher, "Numerical Prediction and Wind Tunnel Experiment for a Pitching Unmanned Combat Air Vehicle," AIAA Paper 2003-0417, 2003.

[3] Elkhoury, M., and Rockwell, D., "Visualized Vortices on Unmanned Combat Air Vehicle Planform: Effect of Reynolds Number," *Journal of Aircraft*, Vol. 41, No. 5, 2004, pp. 1244–1247.
doi:10.2514/1.6290

[4] Gursul, I., Gordnier, R., and Visbal, M., "Unsteady aerodynamics of nonslender delta wings, " *Progress in Aerospace Sciences*, Vol. 41, No. 7, 2005, pp. 515–557.
doi:10.1016/j.paerosci.2005.09.002

[5] Ol, M. V., "The Passage toward Stall of Nonslender Delta Wings at Low Reynolds Number," AIAA Paper 2001-2843, 2001.

[6] Gordnier, R., and Visbal, M., "Higher-Order Compact Difference Scheme Applied to the Simulation of a Low Sweep Delta Wing Flow," AIAA Paper 2003-0620, 2003.

[7] Ol, M. V., and Gharib, M., "Leading-Edge Vortex Structure of Nonslender Delta Wings at Low Reynolds Number," *AIAA Journal*, Vol. 41, No. 1, Jan. 2003, pp. 16–26.
doi:10.2514/2.1930

[8] Taylor, G. S., Schnorbus, T., and Gursul, I., "An Investigation of Vortex Flows over Low Sweep Delta Wings," AIAA Paper 2003-4021, 2003.

[9] Yaniktepe, B., and Rockwell, D., "Flow Structure on a Delta Wing of Low Sweep Angle," *AIAA Journal*, Vol. 42, No. 3, 2004, pp. 513–523.
doi:10.2514/1.1207

[10] Lu, S. F., "Experimental Investigations on the Vortex Structures and Aerodynamics for Flow over 50-Deg Sweep Delta Wings (in Chinese)," Dissertation of Masters Degree, Beijing Univ. of Aeronautics and Astronautics, Beijing, 2005.

[11] Gordnier, R., Visbal, M., Gursul, I., and Wang, Z. J., "Computational and Experimental Investigation of a Nonslender Delta Wing," AIAA Paper 2007-894, 2007.

[12] Zuo, L. X., and Wang, J. J., "Planform and Flexibility on Lift Characteristics for Flow over Low-Aspect Ratio Wings," *Journal of Aerospace Engineering*, Vol. 23, No. 1, 2010, pp. 55–61.
doi:10.1061/(ASCE)0893-1321(2010)23:1(55)

[13] Verhaagen, N. G., and Elsayed, M., "Effect of Leading-Edge Shape on the Flow over $50°$ Delta Wings," AIAA Paper 2008-7330, 2008.

[14] Erickson, G. E., "Water Tunnel Studies of Leading-Edge Vortices," *Journal of Aircraft*, Vol. 19, No. 6, June 1982, pp. 442–448.
doi:10.2514/3.57414

[15] Lowson, M. V., and Riley, A. J., "Vortex Breakdown Control by Delta Wing Geometry," *Journal of Aircraft*, Vol. 32, No. 4, July–Aug. 1995, pp. 832–838.
doi:10.2514/3.46798

[16] Lucking, J. M., "Reynolds Number and Leading-Edge Bluntness Effects on a $65°$ Delta Wing," AIAA Paper 2002-0419, 2002.

[17] Wang, J. J., and Zhang, W., "Experimental Investigations on Leading-Edge Vortex Structures for Flow over Non-Slender Delta Wings," *Chinese Physics Letters*, Vol. 25, No. 7, 2008, pp. 2550–2553.
doi:10.1088/0256-307X/25/7/060

[18] Roe, P., "Approximate Riemann Solvers, Parameter Vectors, and Difference Schemes," *Journal of Computational Physics*, Vol. 43, No. 2, 1981, pp. 357–372.
doi:10.1016/0021-9991(81)90128-5

[19] Wang, J. J., and Lu, S. f., "Effects of Leading-edge Bevels on the Aerodynamic Forces of Non-Slender Delta Wing," *The Aeronautical Journal*, Vol. 109, No. 1098, 2005, pp. 403–407.

[20] Michael, J. H., and Michael, R. M., *Tactics Missiles Aerodynamics (in Chinese)*, Astronautics Publishing Company, Beijing, 1999.

[21] Zhang, H. X., *Structural Analysis of Separated Flows and Vortex Motion (in Chinese)*, National Defense Industry Publishing Company, Beijing, 2005.

[22] Yavuz, M. M., Elkhoury, M., and Rockwell, D., "Near-Surface Topology and Flow Structure on a Delta Wing," *AIAA Journal*, Vol. 42, No. 2, Feb. 2004, pp. 332–340.
doi:10.2514/1.3499